



Article

Monitoring Green Tide in the Yellow Sea Using High-Resolution Imagery and Deep Learning

Weitao Shang ^{1,2,3} , Zhiqiang Gao ^{1,2,*}, Meng Gao ⁴ and Xiaopeng Jiang ^{1,2}

- ¹ CAS Key Laboratory of Coastal Environmental Processes and Ecological Remediation, Yantai Institute of Coastal Zone Research, Chinese Academy of Sciences, Yantai 264003, China
- ² Shandong Key Laboratory of Coastal Environmental Processes, Yantai Institute of Coastal Zone Research, Chinese Academy of Sciences, Yantai 264003, China
- ³ University of Chinese Academy of Sciences, Beijing 100049, China
- ⁴ School of Mathematics and Information Sciences, Yantai University, Yantai 264005, China
- * Correspondence: zqgao@yic.ac.cn; Tel.: +86-535-2109184

Abstract: Green tide beaching events have occurred frequently in the Yellow Sea since 2007, causing a series of ecological and economic problems. Satellite imagery has been widely applied to monitor green tide outbreaks in open water. Traditional satellite sensors, however, are limited by coarse resolution or a low revisit rate, making it difficult to provide timely distribution of information about green tides in the nearshore. In this study, both PlanetScope Super Dove images and unmanned aerial vehicle (UAV) images are used to monitor green tide beaching events on the southern side of Shandong Peninsula, China. A deep learning model (VGGUnet) is used to extract the green tide features and quantify the green tide coverage area or biomass density. Compared with the U-net model, the VGGUnet model has a higher accuracy on the Super Dove and UAV images, with F1-scores of 0.93 and 0.92, respectively. The VGGUnet model is then applied to monitor the distribution of green tide on the beach and in the nearshore water; the results suggest that the VGGUnet model can accurately extract green tide features while discarding other confusing features. By using the Super Dove and UAV images, green tide beaching events can be accurately monitored and are consistent with field investigations. From the perspective of near real-time green tide monitoring, high-resolution imagery combined with deep learning is an effective approach. The findings pave the way for monitoring and tracking green tides in coastal zones, as well as assisting in the prevention and control of green tide disasters.



Citation: Shang, W.; Gao, Z.; Gao, M.; Jiang, X. Monitoring Green Tide in the Yellow Sea Using High-Resolution Imagery and Deep Learning. *Remote Sens.* **2023**, *15*, 1101. <https://doi.org/10.3390/rs15041101>

Academic Editor: Chung-Ru Ho

Received: 9 December 2022

Revised: 7 February 2023

Accepted: 13 February 2023

Published: 17 February 2023



Copyright: © 2023 by the authors. Licensee MDPI, Basel, Switzerland. This article is an open access article distributed under the terms and conditions of the Creative Commons Attribution (CC BY) license (<https://creativecommons.org/licenses/by/4.0/>).

Keywords: Super Dove; unmanned aerial vehicle (UAV); deep learning; green tide; U-net; VGGUnet

1. Introduction

Green tides are marine ecological disasters caused by the excessive proliferation, growth, and accumulation of opportunistic green macroalgae [1], which mostly occur in coastal zones around the world [2,3]. Since 2007, massive green-tide outbreaks have occurred in the Yellow Sea every year from May to August, with *Ulva prolifera* (*U. prolifera*) as the main species [4–7]. Previous studies showed that the Yellow Sea *U. prolifera* green tide is caused by the *Porphyra* aquaculture at Subei Shoal in the southern Yellow Sea [8–10]. When the aquaculture facilities are recovered, large amounts of green algae attached to the ropes are discarded and enter the seawater. These green algae continue to drift northward, driven by wind and waves [11,12]. As a result, in late June and early July, millions of tonnes of green algae biomass accumulate in the offshore waters of the Shandong Peninsula [13–15]. Some green algae are carried ashore by tides and waves and accumulate on the beach of the southern side of Shandong Peninsula, China. During the process of decomposition of these macroalgae, a large amount of hydrogen sulfide gas and ammonia are released, resulting in both ecological risks and human health problems [3,16].

Satellite remote sensing is a useful tool for monitoring and tracking green tides, where timely information extracted from the remote sensing images plays an important part in decision-making and disaster prevention [17–19]. In recent years, there have been many studies focusing on green tide monitoring using the Geostationary Ocean Color Imager (GOCI) and the Moderate Resolution Imaging Spectroradiometer (MODIS) in the Yellow Sea [20,21]. However, because of their coarse resolution, it is difficult to make an accurate estimation of the biomass of green tide on the beaches and in nearshore waters [22,23]. When higher spatial resolution images are available, i.e., Sentinel-2 MSI (10 m), Gaofen-1 WVF (16 m), and Landsat-8 OLI (30 m), small scale features of green tides can be identified and extracted [24,25]. Nonetheless, as their revisiting periods are approximately 4–16 days, it is difficult to realize continuous and real-time monitoring [26,27].

Recent years have seen the development of small, inexpensive satellites (known as CubeSats) that can provide both frequent revisits and high spatial resolution for dynamic monitoring of coastal zones. For instance, the PlanetScope constellation is made up of more than 200 satellites with Dove or Super Dove sensors that can make daily observations for many coastal areas at 3 m resolution [28,29]. It has been demonstrated that Dove imagery is capable of monitoring harmful algal blooms, marine plastic debris, and *Sargassum* mats in coastal areas [30–33]. However, to our best knowledge, there are no reports on using the Dove or Super Dove imagery to monitor green tide beaching events in the Yellow Sea. Meanwhile, unmanned aerial vehicle (UAV) imagery has been applied to detect the distribution of green algae and evaluate the initial biomass of green algae attached to aquaculture rafts because of its strengths of strong flexibility, low cost, and high spatial resolution [34–36]. Thus, it is an indispensable data source for monitoring green tide beaching events.

For remote sensing optical sensors, there are many methods to identify and extract green tide information; the two most commonly used indices are the floating algae index (FAI) and the normalized difference vegetation index (NDVI) [37,38]. Green-tide information can be extracted from these index images by the threshold segmentation method. Because of images affected by clouds, shadows, and variable image backgrounds, the selection of thresholds may require extensive prior knowledge or expert assistance [39,40]. Deep learning provides a possibility to overcome these limitations [41,42]. In the last few years, deep learning has been widely used in areas such as ship detection, macroalgae extraction, and sea ice monitoring [43–45]. For example, Arellano-Verdejo et al. proposed a *Sargassum* extraction algorithm (ERISNet) based on deep learning, which was used to extract *Sargassum* in Mexican coastal waters [46]. Wang et al. used a super-pixel segmentation method and a convolutional neural network model (AlexNet) to extract macroalgae information from UAV images [36]. Gao et al. proposed a deep learning framework known as AlgaeNet for detecting green tide information from SAR and optical imagery [47]. Comparatively, the classic U-net model has been extensively applied in remote sensing image classification due to its efficient network architecture and good image segmentation performance [42,48], so it should also be capable of detecting and extracting green tides on the beaches and in nearshore waters from high-resolution imagery.

Therefore, this paper aims to develop a deep learning approach to detect and extract information about green tides on the beaches and in nearshore waters from Super Dove and UAV images. The remainder of this paper is arranged as follows: firstly, the VGGUnet model is developed and the performance of the model is evaluated; secondly, in the three areas, the spatiotemporal change processes of *U. prolifera* are analyzed on the beach and in nearshore water; and finally, the strengths and weaknesses of this approach and the prevention and control strategies of green tides on beaches and in nearshore waters are discussed.

2. Materials and Methods

2.1. Study Areas

Three study areas (Figure 1a) were chosen for this study (P1 (121.066°E–121.098°E, 36.613°N–36.631°N), P2 (121.129°E–121.178°E, 36.649°N–36.674°N), and P3 (121.281°E–121.298°E, 36.704°N–36.713°N)) on the southern side of the Shandong Peninsula to analyze the changing processes of *U. prolifera* on beaches and in nearshore water. Since the outbreak of the Yellow Sea green tide in 2007, massive amounts of *U. prolifera* have been washed ashore by the tides and waves and accumulated on the beach in the study area every year. The decomposition of stranded *U. prolifera* releases ammonia and hydrogen sulfide gas, posing risks to both the environment and human health. To remove *U. prolifera*, the local government must invest a lot of labor and resources every year. Therefore, it is critical to obtain dynamic information on green algae in a timely and efficient manner in order to help prevent and control green tide disasters. The tides in the study area are dominated by regular semi-diurnal tides, with an average tidal range of 2.24 m and no overt seasonal variations (<http://www.tidescn.com/Tides/1341.html>, accessed on 23 June 2021).

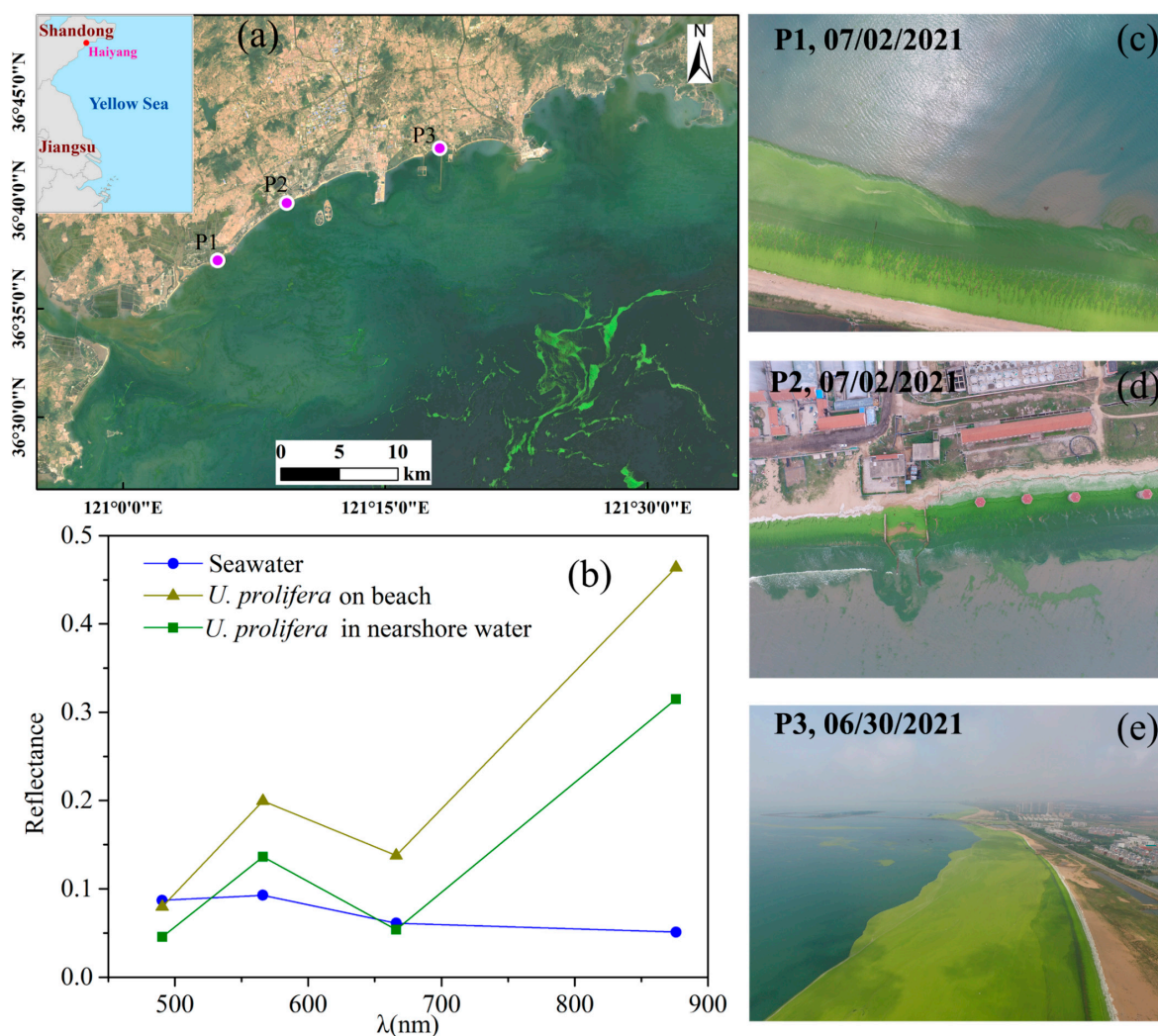


Figure 1. (a) The three research areas are denoted by the letters P1, P2, and P3, respectively. The background image is a Landsat 8 true color image composed of bands 4-3-2 on 23 June 2021 (source: <https://earthexplorer.usgs.gov/>, accessed on 23 June 2021). (b) Spectral reflectance of seawater, *Ulva prolifera* (*U. prolifera*) on the beach, and *U. prolifera* in nearshore water from the Super Dove multispectral image. (c–e) *U. prolifera* on the beach, shot by an unmanned aerial vehicle (UAV) at P1, P2, and P3 study areas.

2.2. Data Preparations

2.2.1. PlanetScope Super Dove Data

More than 200 satellites make up the PlanetScope constellation, which enables the daily delivery of 3 m resolution images of the land surface and coastal waters. The Super Dove 3B image products (surface reflectance data), which contain four-bands (blue, green, red, and near-infrared), were used in this article, and the detailed attributes of the Super Dove sensor are shown in Table 1. A total of 82 four band Super Dove images were acquired between 1 June 2021, and 31 July 2021, from Planet Lab (<https://www.planet.com/explorer/>, accessed on 1 June 2021).

Table 1. Attributes of the Super Dove sensor.

Sensor	Band	Wavelength (nm)	Spatial Resolution (m)	Revisit Cycle (day)
Super Dove	Blue	465–515	3	1
	Green	547–585		
	Red	650–680		
	NIR	845–885		

2.2.2. UAV Data

From 28 June to 8 July 2021, a MATRICE M600 Pro UAV (Figure 2a) (SZ DJI Technology Co., Ltd., Shenzhen, China) equipped with a DJI Zenmuse X3 RGB camera (Figure 2b) was used to take images of *U. prolifera* on the beach and in nearshore water in the three study areas: P1, P2, and P3. The global navigation and positioning system (GPS) on the UAV enables it to record flight altitude and location data for each image. The UAV's maximum flight altitude was set at 150 m. A digital orthophoto map was created using Pix4Dmapper software. Figure 1c–e shows the distribution of *U. prolifera* on the beaches and in nearshore waters in the three study areas (P1, P2, and P3).

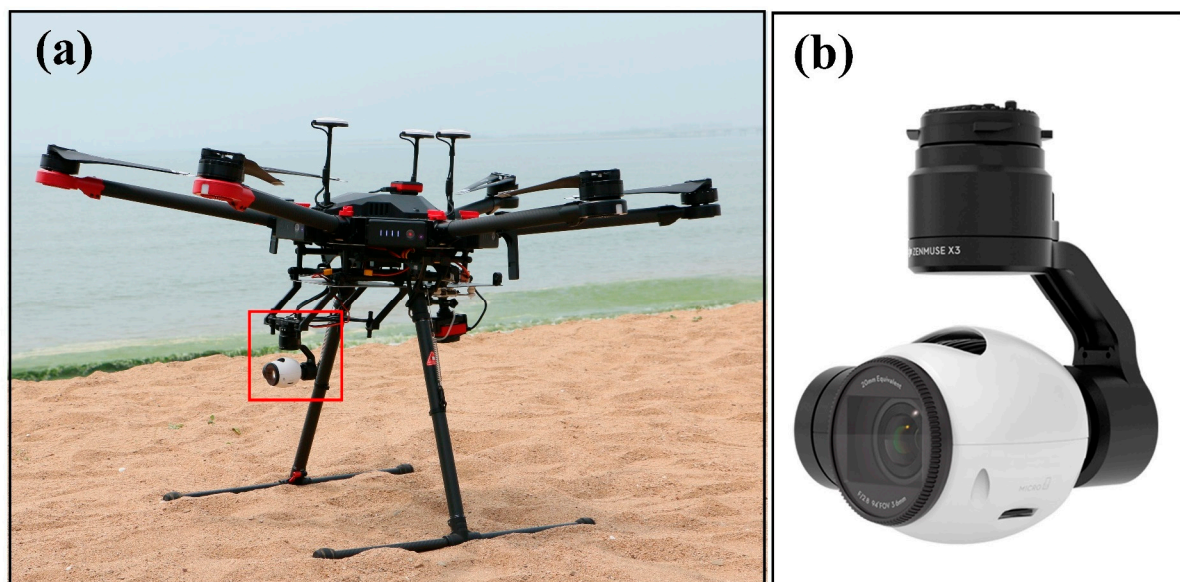


Figure 2. (a) Picture of MATRICE M600 Pro UAV; and (b) DJI Zenmuse X3 RGB camera.

2.3. *U. prolifera* Extraction and Quantification Workflow

2.3.1. *U. prolifera* Extraction Workflow

The workflow for the automatic *U. prolifera* extraction and analysis using the Super Dove and UAV images is shown in Figure 3. When extracting *U. prolifera* information from the Super Dove images, cloud has a significant impact. Therefore, when the image is screened, images with a cloud cover of more than 50% are considered invalid observations.

Clouds have a high reflectance in the blue band of the Super Dove image, making it possible to separate clouds from other ground objects using the threshold method [31]. After numerous tests, the Super Dove blue-band image's pixels with reflectance larger than 0.1 are designated as cloud pixels, and the image is subsequently masked. Because the UAV flies at a low altitude, there is less interference from clouds, so cloud masking has not been considered for UAV images.

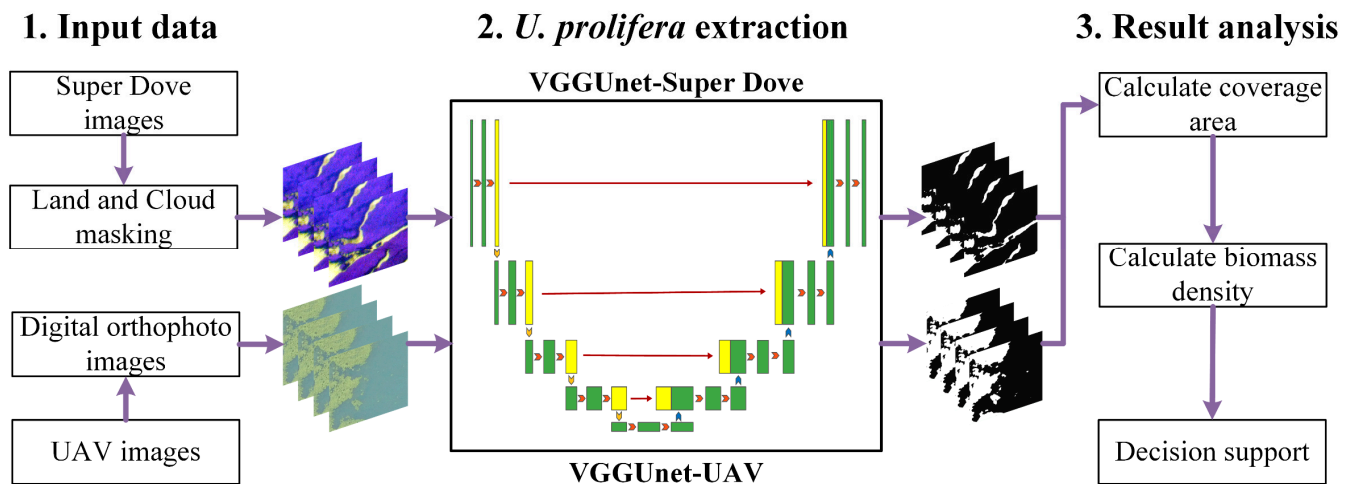


Figure 3. Workflow for the automatic extraction and analysis of *U. prolifera* using images from both the Super Dove and the UAV.

For the Super Dove images, the valid observation data are first generated by land masking and cloud masking. Then the *U. prolifera* pixels are extracted from the Super Dove images using the VGGUnet model (the VGGUnet model is introduced in detail in Section 2.3.2). Finally, the corresponding coverage areas and biomass densities are calculated from all *U. prolifera*-containing pixels.

For the UAV images, the UAV digital orthophoto images are first generated using the Pix4Dmapper software. Then the *U. prolifera* pixels are extracted from the UAV digital orthophoto images using the VGGUnet model. Finally, the corresponding coverage areas and biomass densities are calculated from all *U. prolifera*-containing pixels.

2.3.2. The Construction of the VGGUnet Model Model Architecture

In this study, we used the classical U-net architecture with VGG-16 [49] as the encoder. The U-net model was first proposed in 2015 by Ronneberger et al. [50], mainly for biomedical image segmentation, and was applied in later studies for the feature extraction task of remote sensing images [44,48]. Since VGG-16 was trained on the Image-Net dataset, using VGG-16 as the pre-trained encoder of U-net can effectively improve the performance of segmentation [51]. Therefore, this study used the pre-trained weights obtained from VGG-16 as the encoder of U-net, while the decoder part of U-net remains unchanged. The detailed architecture of the model is shown in Figure 4.

Each convolutional block was normalized using batch normalization [52]. The primary activation function was the rectified linear unit (ReLU). In the final output layer, the sigmoid activation function was used to determine the segmentation results. The VGGUnet model received input from three-band UAV RGB images or four-band multispectral Super Dove images. The model output is the extracted *U. prolifera*-containing pixels.

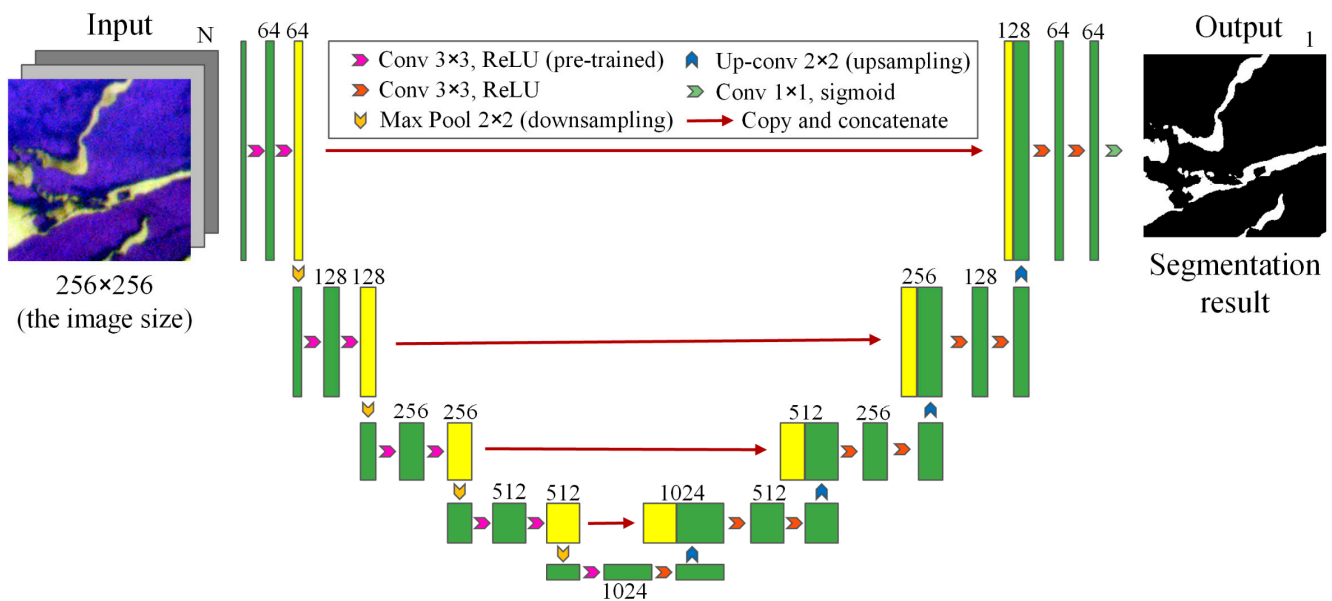


Figure 4. Detailed architecture diagram of the VGGUnet model. The N in the upper-right corner of the input image indicates that the input image has N spectral bands. For instance, the Super Dove image includes four bands (Blue-Green-Red-Nir), and the UAV image has three bands (Blue-Green-Red). The 1 in the upper-right corner of the output image indicates that the output image is a single-band image containing *U. proliferata* pixels.

Training and Accuracy Evaluation of the VGGUnet Model

In the Super Dove and UAV images, the *U. proliferata* has noticeable green patch or stripe features (Figure 1a,c–e). The Labelme software [53] was used to label samples with various *U. proliferata* shapes. A total of 1265 Super Dove sub-images and corresponding labels were selected for the Super Dove images, and 1120 UAV sub-images and corresponding labels were prepared for the UAV RGB images. The datasets were divided into a training set, a verification set, and a testing set according to the ratio of 7:2:1. The data augmentation techniques (including diagonal flip, horizontal flip, and vertical flip) were used to expand the training and validation datasets but not the testing datasets.

In this study, the adaptive moment estimation (Adam) optimizer is used to optimize the model, the binary-cross entropy is used as the loss function, and the initial learning rate is set to 0.001. When there is no improvement in the loss function after two consecutive epochs, the learning rate is dropped by 20% to make a finer adjustment. All models achieved stable performance within 200 epochs in our experiments. Table 2 summarizes the time required for VGGUnet model training on the Super Dove and UAV training datasets. All experiments were carried out on the same server, which was equipped with an Intel (R) Xeon (R) E5-2678 CPU @2.50 GHz and a Nvidia GeForce RTX 3090Ti GPU.

Table 2. Statistics of the time required for VGGUnet model training.

Data	Super Dove	UAV
Number of training datasets	3540	3136
Batch size	32	32
Number of epochs	200	200
Average running time per epoch (s)	78	65
Model training time (h)	4.3	3.6

To evaluate the performance of the constructed VGGUnet model, four evaluation indicators [41,54] were used to quantitatively evaluate the trained model on the testing datasets. In this research, accuracy is defined as the proportion of accurate forecasts to total

predictions. Precision is defined as the ratio of correctly classified positive samples to all samples that were classified as positive. The precision gauges how well the model classifies a sample as positive. Recall is the proportion of positive samples that were accurately identified as being positive among all positive samples. The recall gauges how well the model can identify positive samples. The more positive samples that are found, the greater the recall. The F1-score is the harmonic mean of the precision and recall. It is used to assess a model's binary classification accuracy. The four evaluation indicators are shown in the following formulas:

$$\text{Accuracy} = \frac{\text{TP} + \text{TN}}{\text{TP} + \text{TN} + \text{FP} + \text{FN}} \quad (1)$$

$$\text{Precision} = \frac{\text{TP}}{\text{TP} + \text{FP}} \quad (2)$$

$$\text{Recall} = \frac{\text{TP}}{\text{TP} + \text{FN}} \quad (3)$$

$$\text{F1-score} = \frac{2 \times \text{Precision} \times \text{Recall}}{\text{Precision} + \text{Recall}} \quad (4)$$

where TP, TN, FP, and FN refer to the numbers of true positive samples, true negative samples, false positive samples, and false negative samples, respectively.

To compare the VGGUnet model with traditional threshold-based segmentation methods, the NDVI was used to quantitatively evaluate the green tide extraction results on the Super Dove testing datasets; due to the lack of a near-infrared band, the excess green index (EXG) [55] was used to quantitatively evaluate the green tide extraction results on the UAV testing datasets. The calculation formulas of NDVI and EXG are as follows:

$$\text{NDVI} = \frac{\text{NIR} - \text{R}}{\text{NIR} + \text{R}} \quad (5)$$

$$\text{EXG} = 2 \times \text{G} - \text{R} - \text{B} \quad (6)$$

where NIR, R, G, and B refer to the reflectance or pixel values of the near-infrared, red, green, and blue bands, respectively.

2.3.3. *U. prolifera* Coverage Area and Biomass Density Quantification

In order to distinguish the *U. prolifera* on the beach and in nearshore water, a base map for the three categories seawater, beach, and non-beach land was created by visual interpretation from the relatively low tide Super Dove images between 1 June 2021, and 31 July 2021. Then, the base map was applied to distinguish the *U. prolifera* on the beach and in nearshore water.

The *U. prolifera*-containing pixels were extracted by the VGGUnet model, and then, all *U. prolifera* pixels were summed to obtain the total *U. prolifera* coverage area on the beach and in nearshore water.

From 29 June to 2 July 2021, the biomass densities of *U. prolifera* on the beach were measured at the P1, P2, and P3 study areas (Figure 1a). Six sample quadrats (1 m by 1 m) were selected randomly, and the *U. prolifera* inside the sample quadrat were collected and weighed in each area. The mean wet weight (kg/m²) of *U. prolifera* on the beach was calculated by summing the wet weights of the six samples and dividing by the total number of samples in each area. The mean wet weight (kg/m²) of *U. prolifera* on the beach was 10.34, 14.81, and 14.06 kg/m² at P1, P2, and P3, respectively.

From 29 June to 2 July 2021, the biomass density of *U. prolifera* in nearshore water was measured at the P1, P2, and P3 areas using a fishing net of 0.4 m diameter. Three sites were randomly selected in each area, and each site was measured three times, repeatedly. First, the net was carefully put underneath the *U. prolifera*, then lifted to collect the *U. prolifera* that were within range of the net. The *U. prolifera* samples were put in sample bags and numbered. After shaking off excess water, the wet weight (kg/m²) of each sample was

measured using a digital scale in the laboratory, and the unit biomass of *U. prolifera* was calculated. The mean wet weights of *U. prolifera* in nearshore water were 3.06, 2.74, and 2.67 kg/m² at P1, P2, and P3, respectively.

3. Results

3.1. *U. prolifera* Extraction Performance from the Super Dove and UAV Images

To evaluate the extraction accuracy of the VGGUnet model from Super Dove images, we used 126 Super Dove testing images to quantitatively compare the accuracy of NDVI, the U-net model, and the VGGUnet model. The thresholds of the NDVI are set to 0.51 based on several tests on the Super Dove testing images. Table 3 demonstrates the performance of NDVI, the U-net model, and the VGGUnet model on the Super Dove testing dataset. The NDVI achieved 91.32%, 87.26%, 79.35%, and 0.83 for the four evaluation indicators of accuracy, precision, recall, and F1-score, respectively. The U-net model had an accuracy score of 95.14%, a precision score of 91.13%, a recall score of 90.16%, and an F1-score of 0.91. The VGGUnet model achieved 98.05%, 94.01%, 92.26%, and 0.93 for the four evaluation indicators of accuracy, precision, recall, and F1-score, respectively.

Table 3. The accuracy of *Ulva prolifera* (*U. prolifera*) extraction on Super Dove and unmanned aerial vehicle (UAV) images using different methods.

Input Data	Model	Accuracy (%)	Precision (%)	Recall (%)	F1-Score
Super Dove	NDVI	91.32	87.26	79.35	0.83
	U-net	95.14	91.13	90.16	0.91
	VGGUnet	98.05	94.01	92.26	0.93
UAV	EXG	90.16	85.21	80.43	0.82
	U-net	93.26	90.12	89.82	0.90
	VGGUnet	96.43	93.57	90.53	0.92

Figure 5 shows the *U. prolifera* extraction results from NDVI, the U-net model, and the VGGUnet model on Super Dove images, with most of the *U. prolifera* features being effectively extracted; however, a small number of seawater pixels were misidentified as *U. prolifera* pixels in the NDVI extraction results (Figure 5a–d, annotated by the green rectangle), several small-sized *U. prolifera* patches are missing (Figure 5a–c, annotated by the red rectangle) in the U-net model extraction results, and a few noise signals are misidentified as *U. prolifera* pixels (Figure 5d, annotated by the red rectangle) in the U-net model extraction results. The results showed that, in terms of performance, the VGGnet model outperformed the NDVI and U-net model.

To evaluate the extraction accuracy of the VGGUnet model from UAV images, we used 112 UAV testing images to quantitatively compare the accuracy of EXG, the U-net model, and the VGGUnet model. The thresholds of the EXG are set to 47 based on several tests on the testing images. Table 3 demonstrates the performance of EXG, the U-net model, and the VGGUnet model on the UAV testing dataset. The EXG achieved 90.16%, 85.21%, 80.43%, and 0.82 for the four evaluation indicators of accuracy, precision, recall, and F1-score, respectively. The U-net model had an accuracy score of 93.26%, a precision score of 90.12%, a recall score of 89.82%, and an F1-score of 0.90. The VGGUnet model achieved 96.43%, 93.57%, 90.53%, and 0.92 for the four evaluation indicators of accuracy, precision, recall, and F1-score, respectively.

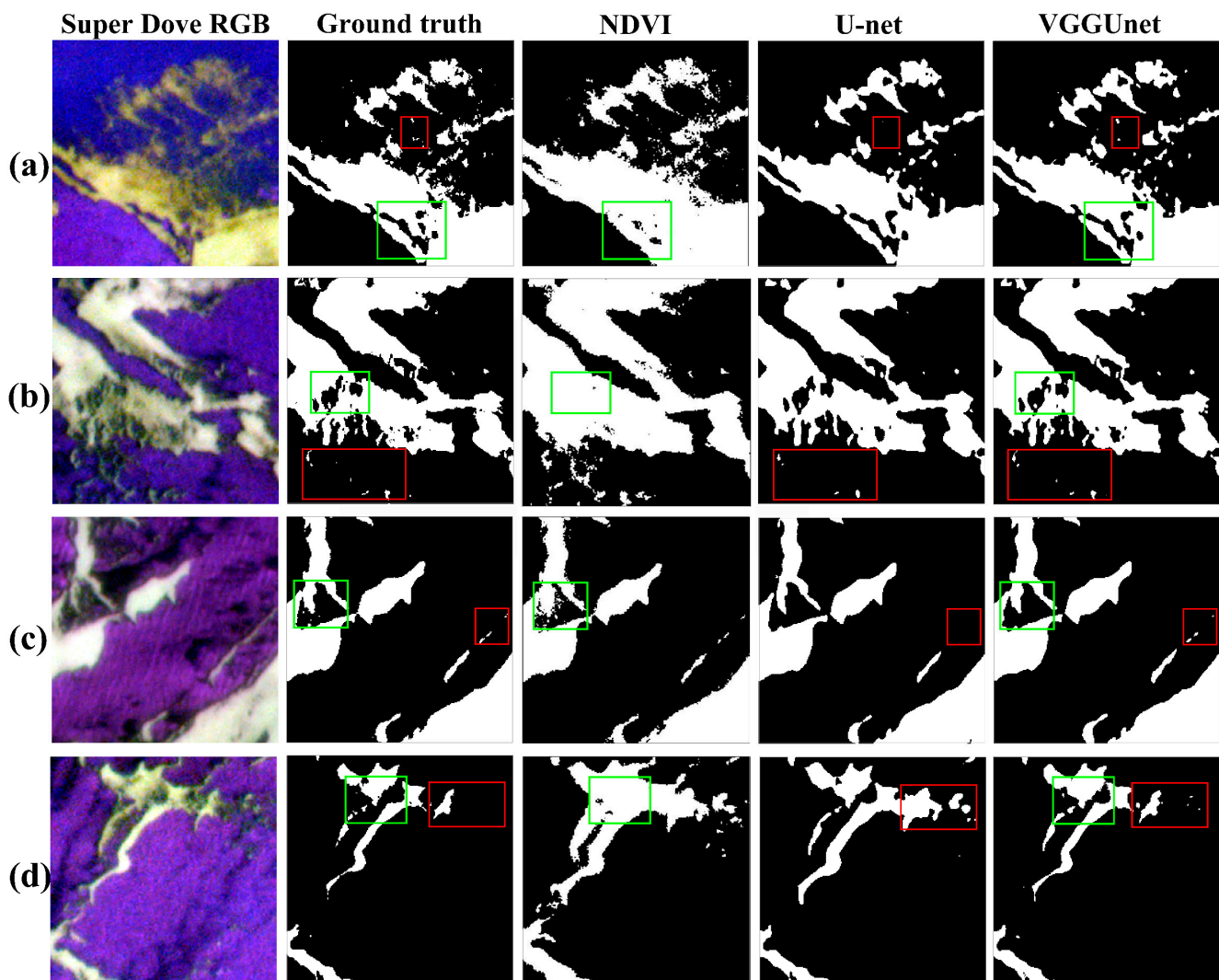


Figure 5. Comparison of *U. prolifera* extraction results from NDVI, the U-net model, and the VGGUnet model on Super Dove images. (a–d) Five test images: the Super Dove RGB image, the ground truth image, the *U. prolifera* extraction result from NDVI, the *U. prolifera* extraction result from the U-net model, and the *U. prolifera* extraction result from the VGGUnet model. The key parts of the comparison between NDVI and the ground truth and the VGGUnet model are shown in red rectangles, while those between the U-net model and the ground truth and the VGGUnet model are shown in green rectangles.

Figure 6 shows the *U. prolifera* extraction results from EXG, the U-net model, and the VGGUnet model on UAV images. The extraction results of *U. prolifera* are satisfactory based on visual inspection, with the vast majority of its features successfully extracted. Nevertheless, a small number of seawater pixels were misidentified as *U. prolifera* pixels in the EXG extraction results (Figure 6a–d, annotated by the green rectangle), several seawater pixels are misidentified as *U. prolifera* pixels (Figure 6a–c, annotated by the red rectangle) in the U-net model extraction results, and a few small-sized *U. prolifera* patches are missing (Figure 6d, annotated by the red rectangle).

Overall, when the VGGUnet model was tested with images from the Super Dove and the UAV, it had an F1-score of 0.93 and 0.92, which suggests that the VGGUnet model could be used to automatically extract *U. prolifera* features.

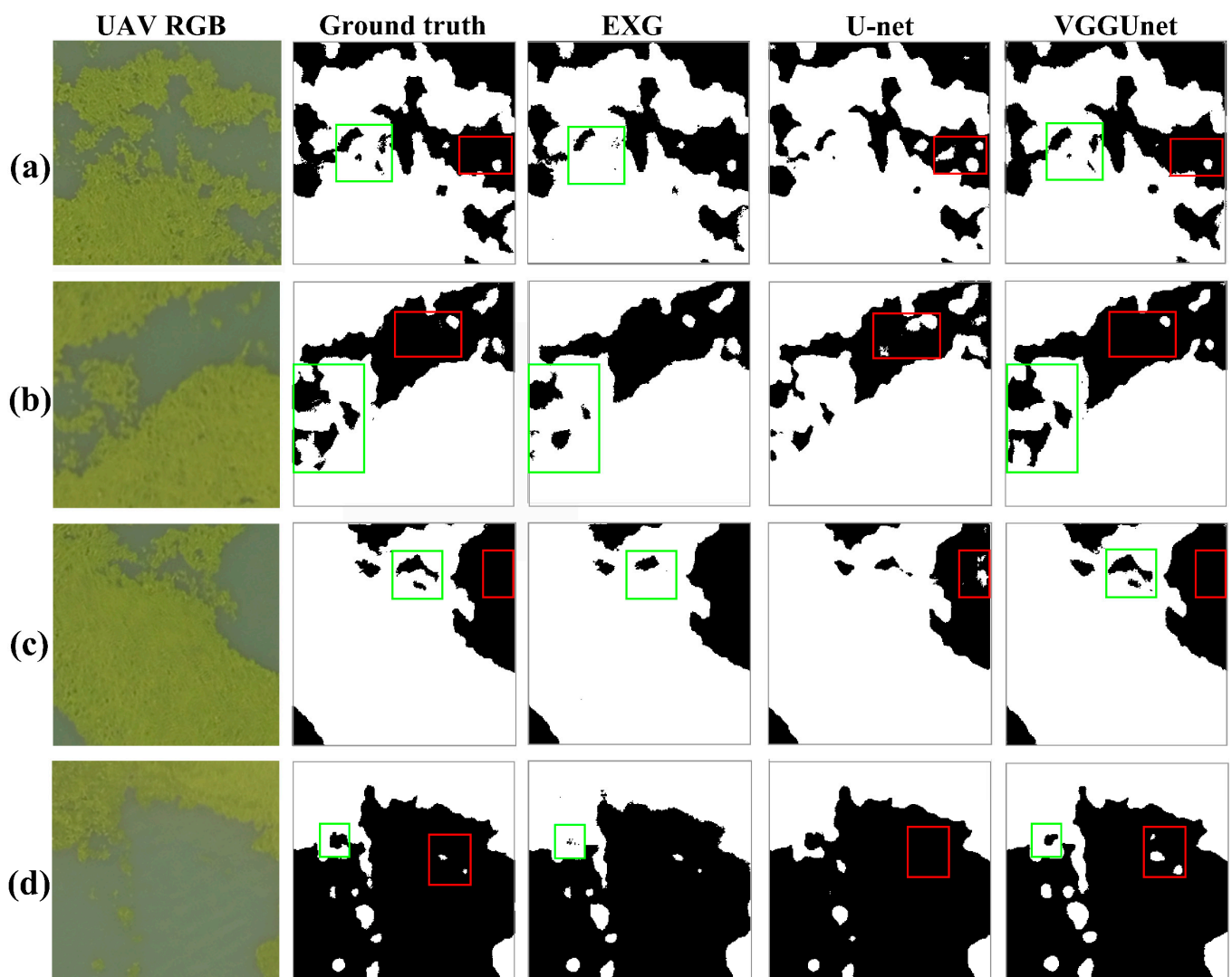


Figure 6. Comparison of *U. prolifera* extraction results from EXG, the U-net model, and the VGGUnet model on UAV images. (a–d) Five test images: the UAV RGB image, the ground truth image, the *U. prolifera* extraction result from EXG, the *U. prolifera* extraction result from the U-net model, and the *U. prolifera* extraction result from the VGGUnet model. The key parts of the comparison between NDVI and the ground truth and the VGGUnet model are shown in red rectangles, while those between the U-net model and the ground truth and the VGGUnet model are shown in green rectangles.

3.2. The Spatiotemporal Change Analysis of *U. prolifera* on the Beach and in Nearshore Water

Figure 7 shows the spatiotemporal changing process of *U. prolifera* on the beach and in nearshore water at P1 and P2 using the VGGUnet model from the Super Dove images. The corresponding coverage area and biomass are shown in Figures 8 and 9, respectively.

For the P1 area, a small amount of *U. prolifera* first appeared on 21 June 2021. Two days later, on 23 June 2021, the area of *U. prolifera* on the beach and in nearshore water increased rapidly from 0.096 km² to 0.51 km². The *U. prolifera* area continued to increase from 0.51 km² on 23 June 2021, to 0.87 km² on 2 July 2021, on the beach and in nearshore water. From 2 July 2021, to 9 July 2021, the *U. prolifera* area decreased gradually from 0.87 km² to 0.46 km². From 21 June 2021, to 9 July 2021, the *U. prolifera* biomass also varied significantly, increasing at first but then decreasing. On 2 July 2021, the daily maximum biomass of *U. prolifera* on the beach and in nearshore water was about 2718 tonnes and 1872 tonnes, respectively, covering 56.4% of the entire beach area in the P1 area.

For the P2 area, a small amount of *U. prolifera* first appeared in nearshore water but not on the beach on 21 June 2021. From 21 June 2021, to 9 July 2021, the *U. prolifera* area

increased gradually from 0.067 km² to 1.28 km². The *U. prolifera* biomass also varied significantly from 21 June 2021, to 9 July 2021. The daily maximum biomass of *U. prolifera* on the beach and in nearshore water was about 4826 tonnes and 3329 tonnes on 9 July 2021 and on 2 July 2021, respectively.

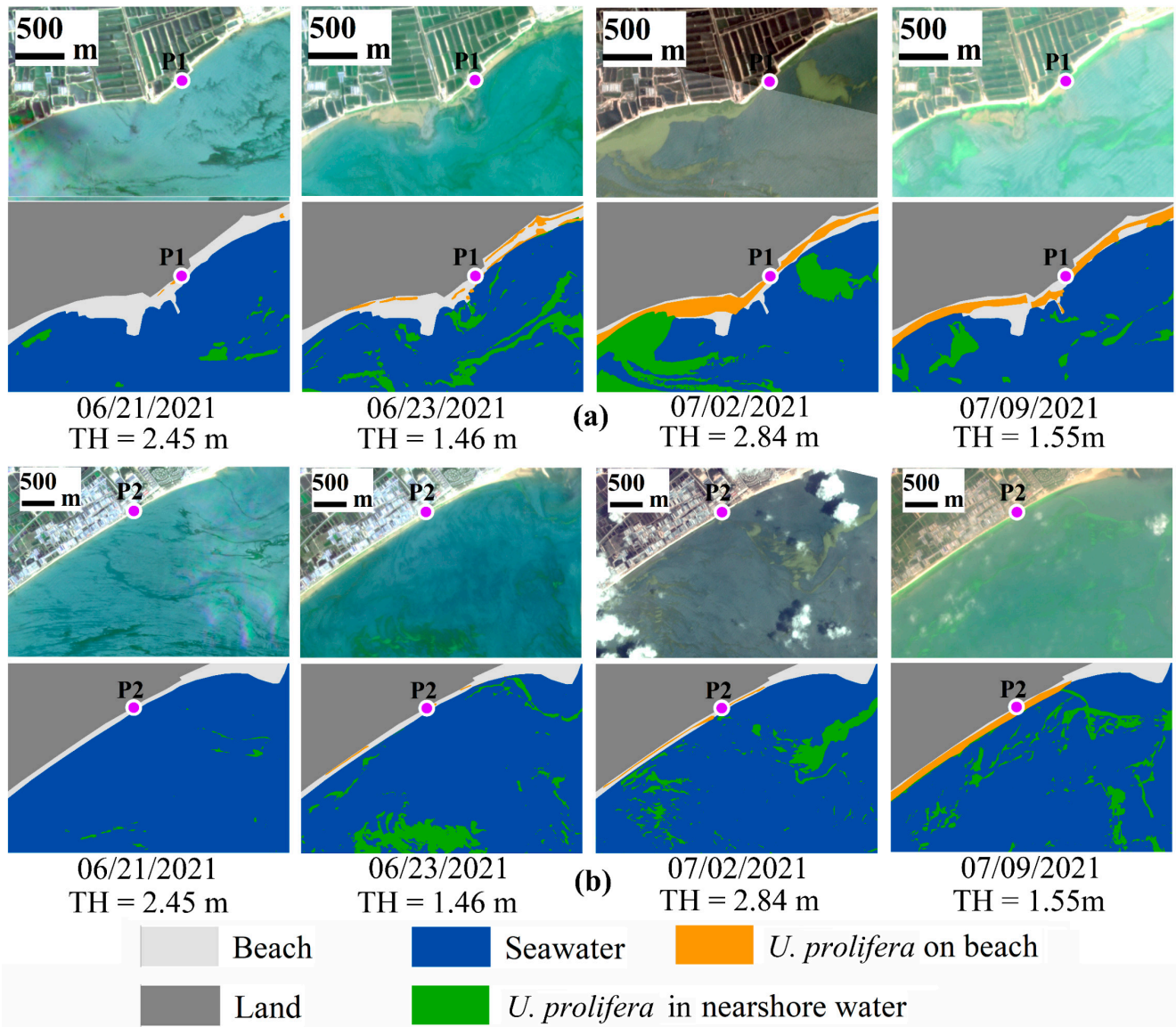


Figure 7. The extraction results of *U. prolifera* on the beach and in nearshore water in the P1 and P2 areas. (a) The spatiotemporal changes of *U. prolifera* on the beach and in nearshore water in the P1 area; (b) the spatiotemporal changes of *U. prolifera* on the beach and in nearshore water in the P2 area. The local tide height (TH) at the time of each image acquisition is marked on the figure.

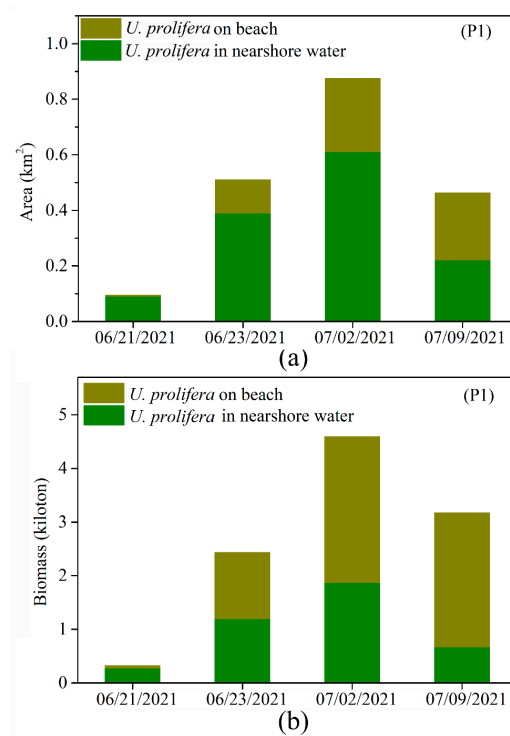


Figure 8. The statistical results for coverage area and biomass of *U. prolifera* in the P1 area. (a) The statistical results for the coverage area of *U. prolifera* on the beach and in nearshore water; (b) the statistical results for the biomass of *U. prolifera* on the beach and in nearshore water.

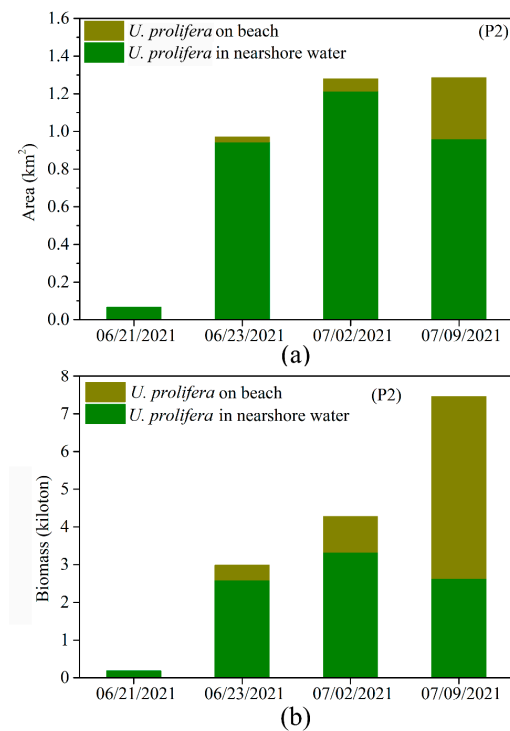


Figure 9. The statistical results for coverage area and biomass of *U. prolifera* in the P2 area. (a) The statistical results for the coverage area of *U. prolifera* on the beach and in nearshore water; (b) the statistical results for the biomass of *U. prolifera* on the beach and in nearshore water.

3.3. Results of Monitoring *U. prolifera* Using the Super Dove Images Combined with the UAV Images

To monitor the dynamic processes of *U. prolifera* on the beach and in nearshore water, the UAV images from 29 to 30 June 2021, and the Super Dove images from 1 July 2021, at the P3 area were collected. The UAV RGB images and Super Dove RGB images are shown in the left column of Figure 10. The extraction results of *U. prolifera* using the VGGUnet model from the UAV images and the Super Dove images are shown in the right column of Figure 10. The corresponding coverage area and biomass data were counted and shown in Figure 11.

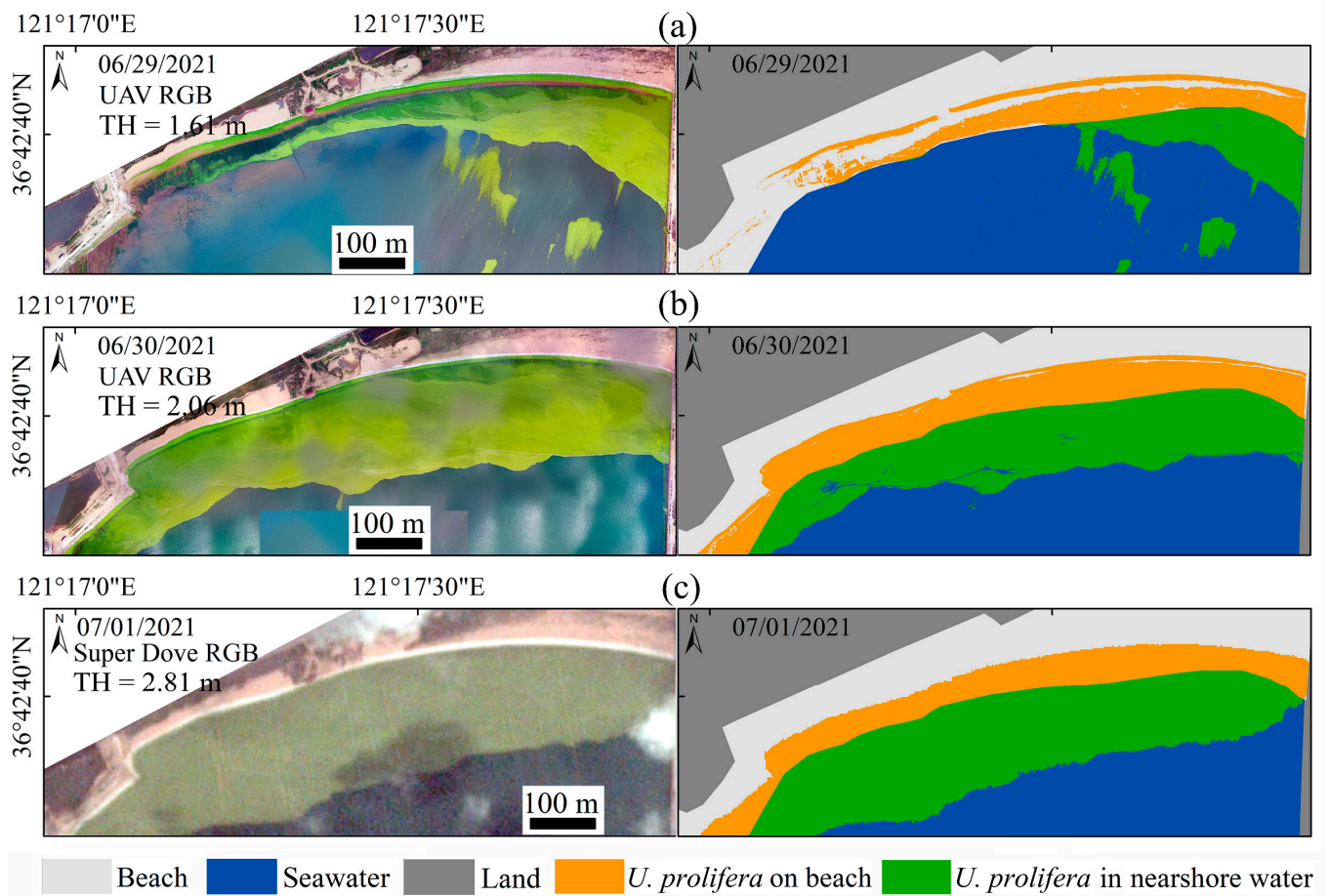


Figure 10. The extraction results of *U. prolifera* on the beach and in nearshore water in the P3 area. (a) The extraction results of *U. prolifera* from a UAV image on 29 June 2021; (b) The extraction results of *U. prolifera* from a UAV image on 30 June 2021; (c) The extraction results of *U. prolifera* from a Super Dove image on 1 July 2021. The local tide height (TH) at the time of each image acquisition is marked on the figure.

From Figure 10, we can clearly see the dynamic processes of *U. prolifera* on the beach and in nearshore water in the P3 area. On 29 June 2021, there was a small amount of *U. prolifera* in the P3 area; the coverage area of *U. prolifera* was 0.063 km² and 0.058 km² on the beach and in nearshore water, respectively. One day later, the coverage area of *U. prolifera* expanded from 0.063 to 0.1 km² on the beach, and the coverage area of *U. prolifera* expanded from 0.058 to 0.15 km² in nearshore water. On 1 July 2021, the coverage area of *U. prolifera* decreased from 0.1 to 0.09 km² on the beach, but the coverage area of *U. prolifera* increased from 0.15 to 0.2 km² in nearshore water. The biomass of *U. prolifera* also varied significantly on the beach and in nearshore water from 29 June 2021, to 1 July 2021, first increasing but

then decreasing. The maximum biomass of *U. prolifera* on the beach and in nearshore water was about 1408 tonnes and 523 tonnes on 30 June 2021, and 1 July 2021, respectively.

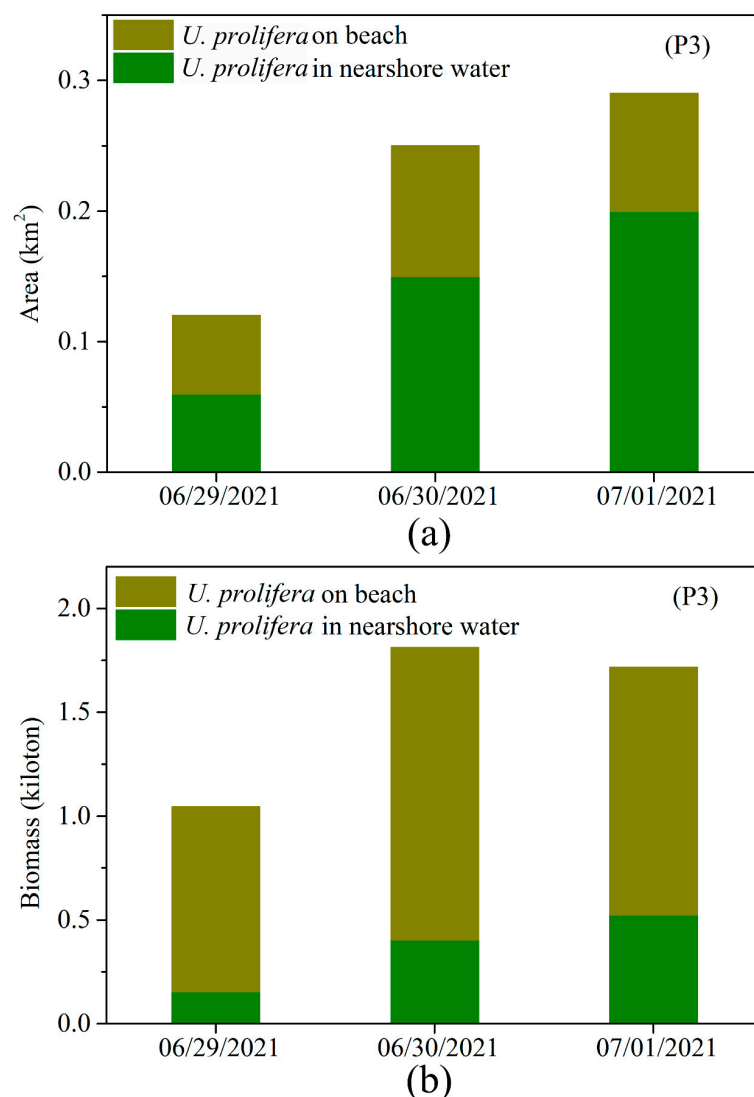


Figure 11. The statistical results for coverage area and biomass of *U. prolifera* in the P3 area. (a) The statistical results for the coverage area of *U. prolifera* on the beach and in nearshore water; (b) the statistical results for the biomass of *U. prolifera* on the beach and in nearshore water.

4. Discussion

4.1. Strengths and Weaknesses of the VGGUnet Model for *U. prolifera* Extraction

By using deep learning technology, we accurately extracted the information of *U. prolifera* on the beach and in nearshore water from the Super Dove and UAV images. This is because deep learning can not only extract the spectral features of remote sensing images but also extract texture features [56,57], so even if the RGB images lack near-infrared bands, the VGGUnet model still shows good performance.

An important advantage of the VGGUnet model is its flexibility. The input to the model can be RGB images (the UAV images) or multispectral images (the Super Dove images). By adjusting the input of the model, the VGGUnet model can be applied to different types of remote sensing images, such as the coarse-resolution MODIS and GOCI images and the high-resolution Sentinel-2 MSI, GF-1 WFV, and Landsat-8 OLI images. By training on different datasets, the VGGUnet model also has promising applications for detecting other features, such as *sargassum* macroalgae blooms and oil slicks [58,59].

Moreover, the VGGUnet model can be directly applied to extract green tide information without selecting a threshold because the weight of the model has been optimized during the model training process. Compared with the traditional threshold-based segmentation method, the deep learning method can reduce some of the possible mistakes caused by choosing the thresholds and improve the accuracy of monitoring green tides [24,42].

One of the disadvantages of deep learning is that it is difficult to interpret and diagnose the results [60,61]. The performance of the model has high requirements for the quality of the training data. The traditional threshold-based green-tide extraction method is intuitive and errors can be easily found, but its use requires some prior knowledge. It is difficult to automatically process many remote sensing images by choosing a fixed threshold. Although deep learning is difficult to interpret and diagnose, superior performing deep learning models are able to extract green-tide information from large amounts of high-resolution data, as long as an appropriate network structure is chosen and training data is carefully selected.

4.2. The VGGUnet Model Application for *U. prolifera* near Real-Time Monitoring and Tracking

Large amounts of *U. prolifera* are deposited on beaches, which not only damages the environment and seriously affects the development of local tourism, but also threatens the health of nearby residents [62,63]. To reduce the impact of *U. prolifera*, local governments need to invest a lot of labor and financial resources clearing the *U. prolifera* deposited on the beach, and the timely and accurate acquisition of the distribution information of *U. prolifera* on the beach and in nearshore water is very important for the government to reasonably arrange the cleanup of *U. prolifera* [64]. In this paper, the Super Dove and UAV images are used to develop a VGGUnet deep learning model for extracting *U. prolifera* from large amounts of remote sensing data. This model can quickly determine where *U. prolifera* is on the beach and in nearshore water, which assists the government do a better job of preventing and dealing with disasters.

The Super Dove images can usually be obtained within one day after the satellite overpass, which provides the possibility for near real-time monitoring of *U. prolifera*, and the UAV can quickly obtain high-resolution images of the monitoring area according to the needs of the mission. Even if satellite remote sensing is affected by clouds and cannot obtain effective data, the UAV can still be used to monitor and track *U. prolifera*. By combining the Super Dove satellite remote sensing images with the UAV images, it should be possible to satisfy the needs of near real-time monitoring and tracking of *U. prolifera* on the beach and in nearshore water.

In addition, the data processing speed is an important factor affecting the near real-time monitoring of *U. prolifera* using the VGGUnet model. Table 4 summarizes the approximate time required to extract *U. prolifera* from Super Dove and UAV images. For a Super Dove image with $14,175 \times 10,404$ pixels, the time required to extract *U. prolifera* using the VGGUnet model is about 2 min (126 s). For a UAV image with $18,000 \times 9000$ pixels, the time required to extract *U. prolifera* using the VGGUnet model is about 3 min (182 s). This makes it possible to extract *U. prolifera* information timely from a large number of high-resolution images, meeting the requirements of near real-time monitoring and tracking of *U. prolifera*.

Table 4. Approximate time required to extract *U. prolifera* from Super Dove and UAV images. The time required is averaged over 16 Super Dove images with $14,175 \times 10,404$ pixels per image and 10 UAV images with $\sim 18,000 \times 9000$ pixels per image.

Data	Super Dove	UAV
The average time required to process each image	126 s	182 s

5. Conclusions

This study developed a green tide detection approach based on the VGGUnet model to extract *U. prolifera* macroalgae from high-resolution Super Dove and UAV images. The

VGGUnet model's performance was evaluated and compared with the U-net model on the Super Dove and UAV testing datasets. For the Super Dove images, the VGGUnet model had a higher accuracy, with an F1-score of 0.93; both the precision and recall were higher than those for the U-net model. Similarly, for the UAV images, the performance of the VGGUnet model (F1-score = 0.92) was superior to that of the U-net model. The VGGUnet model was then applied to extract the distribution of green tide on the beach and in the nearshore water. The features of the green tide could be accurately extracted automatically from a great deal of high-resolution imagery. This provides an effective tool for extracting green tide information from the Super Dove and UAV images and can meet the needs for near real-time green tide monitoring on beaches and in nearshore waters. Furthermore, this method can be extended to other high-resolution remote sensing images, such as Sentinel-2 MSI, GF-1 WFV, and Landsat-8 OLI images. In addition, the VGGUnet model also has promising applications for detecting other features, such as *sargassum* macroalgae blooms and oil slicks. In the future, multi-source remote sensing images and deep learning methods could be used to monitor the occurrence, development, and disappearance processes of the Yellow Sea green tide, which can provide help for the prevention and control of green tides.

Author Contributions: Conceptualization, W.S.; methodology, W.S. and M.G.; software, W.S.; validation, W.S. and X.J.; formal analysis, W.S. and M.G.; investigation, W.S. and X.J.; resources, W.S. and X.J.; data curation, W.S.; writing—original draft preparation, W.S.; writing—review and editing, W.S., M.G. and X.J.; visualization, W.S.; supervision, Z.G.; project administration, Z.G.; funding acquisition, Z.G. All authors have read and agreed to the published version of the manuscript.

Funding: This research was funded by The National Natural Science Foundation of China, grant number 41876107 and 31570423; the National Key R&D Program of China, grant number 2019YFD0900705; the Key Program of Shandong Natural Science Foundation, grant number ZR2020KF031; Fundamental Research Projects of Science and Technology Innovation and development Plan in Yantai City, grant number 2022YTJC06003045.

Acknowledgments: The authors would like to thank Planet Labs, Inc. for providing Super Dove satellite remote sensing data.

Conflicts of Interest: The authors declare no conflict of interest.

References

1. Valiela, I.; McClelland, J.; Hauxwell, J.; Behr, P.J.; Hersh, D.; Foreman, K. Macroalgal blooms in shallow estuaries: Controls and ecophysiological and ecosystem consequences. *Limnol. Oceanogr.* **1997**, *42*, 1105–1118. [[CrossRef](#)]
2. Merceron, M.; Antoine, V.; Aubry, I.; Morand, P. In situ growth potential of the subtidal part of green tide forming *Ulva* spp. stocks. *Sci. Total Environ.* **2007**, *384*, 293–305. [[CrossRef](#)] [[PubMed](#)]
3. Smetacek, V.; Zingone, A. Green and golden seaweed tides on the rise. *Nature* **2013**, *504*, 84–88. [[CrossRef](#)] [[PubMed](#)]
4. Liu, D.; Keesing, J.K.; Xing, Q.; Shi, P. World's largest macroalgal bloom caused by expansion of seaweed aquaculture in China. *Mar. Pollut. Bull.* **2009**, *58*, 888–895. [[CrossRef](#)]
5. Xu, Q.; Zhang, H.; Ju, L.; Chen, M. Interannual variability of *Ulva prolifera* blooms in the Yellow Sea. *Int. J. Remote Sens.* **2014**, *35*, 4099–4113. [[CrossRef](#)]
6. Liu, D.; Keesing, J.K.; Dong, Z.; Zhen, Y.; Di, B.; Shi, Y.; Fearn, P.; Shi, P. Recurrence of the world's largest green-tide in 2009 in Yellow Sea, China: *Porphyra yezoensis* aquaculture rafts confirmed as nursery for macroalgal blooms. *Mar. Pollut. Bull.* **2010**, *60*, 1423–1432. [[CrossRef](#)]
7. Keesing, J.K.; Liu, D.; Fearn, P.; Garcia, R. Inter- and intra-annual patterns of *Ulva prolifera* green tides in the Yellow Sea during 2007–2009, their origin and relationship to the expansion of coastal seaweed aquaculture in China. *Mar. Pollut. Bull.* **2011**, *62*, 1169–1182. [[CrossRef](#)]
8. Huo, Y.; Zhang, J.; Chen, L.; Hu, M.; Yu, K.; Chen, Q.; He, Q.; He, P. Green algae blooms caused by *Ulva prolifera* in the southern Yellow Sea: Identification of the original bloom location and evaluation of biological processes occurring during the early northward floating period. *Limnol. Oceanogr.* **2013**, *58*, 2206–2218. [[CrossRef](#)]
9. Zhang, J.; Huo, Y.; Wu, H.; Yu, K.; Kim, J.K.; Yarish, C.; Qin, Y.; Liu, C.; Xu, R.; He, P. The origin of the *Ulva* macroalgal blooms in the Yellow Sea in 2013. *Mar. Pollut. Bull.* **2014**, *89*, 276–283. [[CrossRef](#)]
10. Liu, X.; Li, Y.; Wang, Z.; Zhang, Q.; Cai, X. Cruise observation of *Ulva prolifera* bloom in the southern Yellow Sea, China. *Estuar. Coast. Shelf Sci.* **2015**, *163*, 17–22. [[CrossRef](#)]
11. Son, Y.B.; Choi, B.J.; Kim, Y.H.; Park, Y.G. Tracing floating green algae blooms in the Yellow Sea and the East China Sea using GOCI satellite data and Lagrangian transport simulations. *Remote Sens. Environ.* **2015**, *156*, 21–33. [[CrossRef](#)]

12. Hu, P.; Liu, Y.; Hou, Y.; Yi, Y. An early forecasting method for the drift path of green tides: A case study in the Yellow Sea, China. *Int. J. Appl. Earth Obs. Geoinf.* **2018**, *71*, 121–131. [[CrossRef](#)]
13. Hu, L.; Hu, C.; He, M. Remote estimation of biomass of *Ulva prolifera* macroalgae in the Yellow Sea. *Remote Sens. Environ.* **2017**, *192*, 217–227. [[CrossRef](#)]
14. Hu, L.; Zeng, K.; Hu, C.; He, M. On the remote estimation of *Ulva prolifera* areal coverage and biomass. *Remote Sens. Environ.* **2019**, *223*, 194–207. [[CrossRef](#)]
15. Xiao, Y.; Zhang, J.; Cui, T.; Gong, J.; Liu, R.; Chen, X.; Liang, X. Remote sensing estimation of the biomass of floating *Ulva prolifera* and analysis of the main factors driving the interannual variability of the biomass in the Yellow Sea. *Mar. Pollut. Bull.* **2019**, *140*, 330–340. [[CrossRef](#)]
16. Ye, N.; Zhang, X.; Mao, Y.; Liang, C.; Xu, D.; Zou, J.; Zhuang, Z.; Wang, Q. ‘Green tides’ are overwhelming the coastline of our blue planet: Taking the world’s largest example. *Ecol. Res.* **2011**, *26*, 477–485. [[CrossRef](#)]
17. Qi, L.; Hu, C.; Xing, Q.; Shang, S. Long-term trend of *Ulva prolifera* blooms in the western Yellow Sea. *Harmful Algae* **2016**, *58*, 35–44. [[CrossRef](#)]
18. Cao, Y.; Wu, Y.; Fang, Z.; Cui, X.; Liang, J.; Song, X. Spatiotemporal Patterns and Morphological Characteristics of *Ulva prolifera* Distribution in the Yellow Sea, China in 2016–2018. *Remote Sens.* **2019**, *11*, 445. [[CrossRef](#)]
19. Zhang, J.; Shi, J.; Gao, S.; Huo, Y.; Cui, J.; Shen, H.; Liu, G.; He, P. Annual patterns of macroalgal blooms in the Yellow Sea during 2007–2017. *PLoS ONE* **2019**, *14*, e0210460. [[CrossRef](#)]
20. Cui, T.; Zhang, J.; Sun, L.; Jia, Y.; Zhao, W.; Wang, Z.; Meng, J. Satellite monitoring of massive green macroalgae bloom (GMB): Imaging ability comparison of multi-source data and drifting velocity estimation. *Int. J. Remote Sens.* **2012**, *33*, 5513–5527. [[CrossRef](#)]
21. Son, Y.B.; Min, J.E.; Ryu, J.H. Detecting Massive Green Algae (*Ulva prolifera*) Blooms in the Yellow Sea and East China Sea using Geostationary Ocean Color Imager (GOCI) Data. *Ocean Sci. J.* **2012**, *47*, 359–375. [[CrossRef](#)]
22. Xiao, Y.; Zhang, J.; Cui, T. High-precision extraction of nearshore green tides using satellite remote sensing data of the Yellow Sea, China. *Int. J. Remote Sens.* **2017**, *38*, 1626–1641. [[CrossRef](#)]
23. Cui, T.W.; Liang, X.J.; Gong, J.L.; Tong, C.; Xiao, Y.F.; Liu, R.J.; Zhang, X.; Zhang, J. Assessing and refining the satellite-derived massive green macro-algal coverage in the Yellow Sea with high resolution images. *ISPRS J. Photogramm. Remote Sens.* **2018**, *144*, 315–324. [[CrossRef](#)]
24. Wang, M.; Hu, C. Automatic Extraction of Sargassum Features From Sentinel-2 MSI Images. *IEEE Trans. Geosci. Remote Sens.* **2021**, *59*, 2579–2597. [[CrossRef](#)]
25. Li, D.; Gao, Z.; Song, D. Analysis of environmental factors affecting the large-scale long-term sequence of green tide outbreaks in the Yellow Sea. *Estuar. Coast. Shelf Sci.* **2021**, *260*, 107504. [[CrossRef](#)]
26. Li, D.; Gao, Z.; Xu, F. Research on the dissipation of green tide and its influencing factors in the Yellow Sea based on Google Earth Engine. *Mar. Pollut. Bull.* **2021**, *172*, 112801. [[CrossRef](#)]
27. Li, D.; Gao, Z.; Wang, Z. Analysis of the reasons for the outbreak of Yellow Sea green tide in 2021 based on long-term multi-source data. *Mar. Environ. Res.* **2022**, *178*, 105649. [[CrossRef](#)]
28. Wicaksono, P.; Lazuardi, W. Assessment of PlanetScope images for benthic habitat and seagrass species mapping in a complex optically shallow water environment. *Int. J. Remote Sens.* **2018**, *39*, 5739–5765. [[CrossRef](#)]
29. Yamano, H.; Sakuma, A.; Harii, S. Coral-spawn slicks: Reflectance spectra and detection using optical satellite data. *Remote Sens. Environ.* **2020**, *251*, 112058. [[CrossRef](#)]
30. Kikaki, A.; Karantzas, K.; Power, C.A.; Raitsos, D.E. Remotely Sensing the Source and Transport of Marine Plastic Debris in Bay Islands of Honduras (Caribbean Sea). *Remote Sens.* **2020**, *12*, 1727. [[CrossRef](#)]
31. Wang, M.; Hu, C. Satellite remote sensing of pelagic *Sargassum* macroalgae: The power of high resolution and deep learning. *Remote Sens. Environ.* **2021**, *264*, 112631. [[CrossRef](#)]
32. Liu, S.; Glamore, W.; Tamburic, B.; Morrow, A.; Johnson, F. Remote sensing to detect harmful algal blooms in inland waterbodies. *Sci. Total Environ.* **2022**, *851*, 158096. [[CrossRef](#)] [[PubMed](#)]
33. Shin, J.S.; Jo, Y.H.; Ryu, J.H.; Khim, B.K.; Kim, S.M. High Spatial-Resolution Red Tide Detection in the Southern Coast of Korea Using U-Net from PlanetScope Imagery. *Sensors* **2021**, *21*, 4447. [[CrossRef](#)] [[PubMed](#)]
34. Jiang, X.; Gao, M.; Gao, Z. A novel index to detect green-tide using UAV-based RGB imagery. *Estuar. Coast. Shelf Sci.* **2020**, *245*, 106943. [[CrossRef](#)]
35. Jiang, X.; Gao, Z.; Zhang, Q.; Wang, Y.; Tian, X.; Shang, W.; Xu, F. Remote sensing methods for biomass estimation of green algae attached to nursery-nets and raft rope. *Mar. Pollut. Bull.* **2020**, *150*, 110678. [[CrossRef](#)]
36. Wang, S.; Liu, L.; Qu, L.; Yu, C.; Sun, Y.; Gao, F.; Dong, J. Accurate *Ulva prolifera* regions extraction of UAV images with superpixel and CNNs for ocean environment monitoring. *Neurocomputing* **2019**, *348*, 158–168. [[CrossRef](#)]
37. Rouse, J.W.; Haas, R.H.; Schell, J.A.; Deering, D.W. Monitoring vegetation systems in the Great Plains with ERTS. In *3rd Earth Resources Technology Satellite-1 Symposium*; NASA: Washington, DC, USA, 1973; pp. 309–317.
38. Hu, C. A novel ocean color index to detect floating algae in the global oceans. *Remote Sens. Environ.* **2009**, *113*, 2118–2129. [[CrossRef](#)]
39. Hu, C.; Li, D.; Chen, C.; Ge, J.; Muller-Karger, F.E.; Liu, J.; Yu, F.; He, M. On the recurrent *Ulva prolifera* blooms in the Yellow Sea and East China Sea. *J. Geophys. Res. Oceans* **2010**, *115*, C05017. [[CrossRef](#)]

40. Shi, W.; Wang, M. Green macroalgae blooms in the Yellow Sea during the spring and summer of 2008. *J. Geophys. Res. Oceans* **2009**, *114*, C12010. [[CrossRef](#)]
41. Schmidhuber, J. Deep learning in neural networks: An overview. *Neural Netw.* **2015**, *61*, 85–117. [[CrossRef](#)]
42. Li, X.; Liu, B.; Zheng, G.; Ren, Y.; Zhang, S.; Liu, Y.; Gao, L.; Liu, Y.; Zhang, B.; Wang, F. Deep-learning-based information mining from ocean remote-sensing imagery. *Natl. Sci. Rev.* **2020**, *7*, 1584–1605. [[CrossRef](#)]
43. Tang, J.; Deng, C.; Huang, G.; Zhao, B. Compressed-Domain Ship Detection on Spaceborne Optical Image Using Deep Neural Network and Extreme Learning Machine. *IEEE Trans. Geosci. Remote Sens.* **2015**, *53*, 1174–1185. [[CrossRef](#)]
44. Ma, L.; Liu, Y.; Zhang, X.; Ye, Y.; Yin, G.; Johnson, B.A. Deep learning in remote sensing applications: A meta-analysis and review. *ISPRS J. Photogramm. Remote Sens.* **2019**, *152*, 166–177. [[CrossRef](#)]
45. Ren, Y.; Li, X.; Yang, X.; Xu, H. Development of a Dual-Attention U-Net Model for Sea Ice and Open Water Classification on SAR Images. *IEEE Geosci. Remote Sens. Lett.* **2022**, *19*, 1–5. [[CrossRef](#)]
46. Arellano-Verdejo, J.; Lazcano-Hernandez, H.E.; Cabanillas-Teran, N. ERISNet: Deep neural network for *Sargassum* detection along the coastline of the Mexican Caribbean. *PeerJ* **2019**, *7*, e6842. [[CrossRef](#)]
47. Gao, L.; Li, X.; Kong, F.; Yu, R.; Guo, Y.; Ren, Y. AlgaeNet: A Deep-Learning Framework to Detect Floating Green Algae From Optical and SAR Imagery. *IEEE J. Sel. Top. Appl. Earth Obs. Remote Sens.* **2022**, *15*, 2782–2796. [[CrossRef](#)]
48. Vladimir, I.; Alexey, S. Ternaunet: U-net with vgg11 encoder pre-trained on imagenet for image segmentation. *arXiv* **2018**, arXiv:1801.05746.
49. Karen, S.; Andrew, Z. Very deep convolutional networks for large-scale image recognition. *arXiv* **2014**, arXiv:1409.1556.
50. Ronneberger, O.; Fischer, P.; Brox, T. U-Net: Convolutional Networks for Biomedical Image Segmentation. In Proceedings of the 18th International Conference on Medical Image Computing and Computer-Assisted Intervention (MICCAI), Munich, Germany, 5–9 October 2015; pp. 234–241.
51. Iglovikov, V.; Mushinskiy, S.; Osin, V. Satellite imagery feature detection using deep convolutional neural network: A kaggle competition. *arXiv* **2017**, arXiv:1706.06169.
52. Lofte, S.; Szegedy, C. Batch Normalization: Accelerating Deep Network Training by Reducing Internal Covariate Shift. *arXiv* **2015**, arXiv:1502.03167.
53. Russell, B.C.; Torralba, A.; Murphy, K.P.; Freeman, W.T. LabelMe: A database and web-based tool for image annotation. *Int. J. Comput. Vis.* **2008**, *77*, 157–173. [[CrossRef](#)]
54. Minar, M.R.; Naher, J. Recent advances in deep learning: An overview. *arXiv* **2018**, arXiv:1807.08169.
55. Woebbecke, D.M.; Meyer, G.E.; Vonbargen, K.; Mortensen, D.A. Color Indices for Weed Identification Under Various Soil, Residue, and Lighting Conditions. *Trans. ASAE* **1995**, *38*, 259–269. [[CrossRef](#)]
56. Cheng, G.; Han, J. A survey on object detection in optical remote sensing images. *ISPRS J. Photogramm. Remote Sens.* **2016**, *117*, 11–28. [[CrossRef](#)]
57. Cheng, G.; Han, J.; Lu, X. Remote Sensing Image Scene Classification: Benchmark and State of the Art. *Proc. IEEE* **2017**, *105*, 1865–1883. [[CrossRef](#)]
58. Qi, L.; Hu, C.; Wang, M.; Shang, S.; Wilson, C. Floating Algae Blooms in the East China Sea. *Geophys. Res. Lett.* **2017**, *44*, 11501–11509. [[CrossRef](#)]
59. Bianchi, F.M.; Espeseth, M.M.; Borch, N. Large-Scale Detection and Categorization of Oil Spills from SAR Images with Deep Learning. *Remote Sens.* **2020**, *12*, 2260. [[CrossRef](#)]
60. Zhu, X.; Tuia, D.; Mou, L.; Xia, G.; Zhang, L.; Xu, F.; Fraundorfer, F. Deep Learning in Remote Sensing. *IEEE Geosci. Remote Sens. Mag.* **2017**, *5*, 8–36. [[CrossRef](#)]
61. Yuan, Q.; Shen, H.; Li, T.; Li, Z.; Li, S.; Jiang, Y.; Xu, H.; Tan, W.; Yang, Q.; Wang, J.; et al. Deep learning in environmental remote sensing: Achievements and challenges. *Remote Sens. Environ.* **2020**, *241*, 111716. [[CrossRef](#)]
62. Wang, C.; Yu, R.; Zhou, M. Acute toxicity of live and decomposing green alga *Ulva (Enteromorpha) prolifera* to abalone *Haliotis discus hannai*. *Chin. J. Oceanol. Limnol.* **2011**, *29*, 541–546. [[CrossRef](#)]
63. Wang, C.; Yu, R.; Zhou, M. Effects of the decomposing green macroalga *Ulva (Enteromorpha) prolifera* on the growth of four red-tide species. *Harmful Algae* **2012**, *16*, 12–19. [[CrossRef](#)]
64. Zhang, Y.; He, P.; Li, H.; Li, G.; Liu, J.; Jiao, F.; Zhang, J.; Huo, Y.; Shi, X.; Su, R.; et al. *Ulva prolifera* green-tide outbreaks and their environmental impact in the Yellow Sea, China. *Natl. Sci. Rev.* **2019**, *6*, 825–838. [[CrossRef](#)] [[PubMed](#)]

Disclaimer/Publisher’s Note: The statements, opinions and data contained in all publications are solely those of the individual author(s) and contributor(s) and not of MDPI and/or the editor(s). MDPI and/or the editor(s) disclaim responsibility for any injury to people or property resulting from any ideas, methods, instructions or products referred to in the content.